

# Noninvasive Experimental Determination of Charge and Voltage Distributions on an Active Surface

Kuang Yi Chen, Paul David Biernacki, Steve Buchheit, and Alan Rolf Mickelson

**Abstract**—Optical sampling has been employed to obtain the charge and voltage distributions on both a self oscillating active antenna and a power combining oscillating array of such active antennas. Various oscillating arrays have been fabricated on GaAs substrates, and the microwave characteristics of these active structures were tested before the optical sampling measurements were performed. The results of optical sampling measurements have revealed some interesting characteristics of both the individual antenna and array operation. It was noted that the charge and voltage distributions of a single isolated oscillating antenna were quite similar to those measured on an oscillating antenna in an array. Along with this, no edge effects were observed in the finite arrays. The charge and voltage distributions repeated smoothly in periods less than a wavelength with the excess phase necessary to achieve 180 degrees per cell being taken up by a large phase jump across each transistor, despite the fact that each transistor has dimension much smaller than the free space wavelength of the oscillation. Some analytical modeling results are presented to try to put the results into perspective.

## I. INTRODUCTION

THE MOST ubiquitous microwave circuit diagnostic technique, that of network analysis, measures only terminal characteristics. In a frequency limit where elements can be considered as lumped, this information is enough for full circuit characterization. However, with increasing frequency, circuits become increasingly distributed and the detailed placement of elements can determine terminal performance. Electromagnetic solvers can be used to try to predict terminal characteristics in such cases. These simulations predict much more than just the terminal characteristics. They also predict details of internal charge distributions on the lines. There is, unfortunately, no commonly used technique to verify these theoretical predictions.

Various forms of electrooptic sampling have been developed for on-chip metrology. During the past several years, our emphasis has been concentrated on the direct electrooptic sampling technique, its calibration [1], its use to verify electromagnetic models of both microstrip circuits [2] and coplanar waveguide (CPW) circuits [3].

The basic idea behind optical sampling is that an electric field applied to an electrooptic crystal will cause a change in the index of refraction of the crystal. Depending on crystal type and orientation, the integrated change in the index of

refraction as sensed by an optical ray in traveling through the substrate can be read out by placing the substrate either in an arm of an interferometer or in a polarimeter. This integrated change of the index of refraction is then proportional to the voltage difference along that path, as the local index change is linearly proportional to the local electric field. Generally in a microwave circuit, the charge density to be determined is the surface charge density on the electrodes. Given this surface charge density (under the assumption that it is the dominant charge density), one can relate the potential difference in the circuit to this density through the appropriate Green's function. In this manner, a two-dimensional (2-D) optical sampling map can yield both the potential distribution and the surface charge distribution within a microwave circuit. Such mappings contain a wealth of information about the electromagnetic operation of such a circuit. The measurement data can serve as a test of any electromagnetic simulation of such a circuit. In [2] and [3], such comparisons are performed and shown to be in agreement for the simple passive guided wave structures considered. In this work, we will apply the optical sampling technique to an active power combining array.

The paper is organized as follows. In Section II, optical sampling will be discussed in some detail. In Section III, the requisite mathematical relations between these quantities will be derived. In Section IV, the test structure used in this work will be described, and results of its electrical characterization presented. The results of the sampling measurements will be presented in Section V. Section VI is devoted to a discussion of the sampling results and the operation of the test structure.

## II. OPTICAL SAMPLING AND WHAT IT MEASURES

As has recently been shown, the direct optical sampling technique can be used in concert with a calibration algorithm [1] for 2-D mapping of charge and potential distributions in both microstrip [2] and coplanar waveguide circuits [3]. The technique has good spatial resolution ( $<10\ \mu\text{m}$ ) and with proper calibration can exhibit a 50 dB dynamic range for certain substrates. In this sense, optical sampling can provide one with a wealth of spatial information not amenable to "standard" characterization techniques. Further, the optical sampling technique is noninvasive (at least as far as the optical focusing system is kept sufficiently far away from the test structure), as neither charge nor microwave energy need be extracted from the circuit under test, whereas probing techniques must by nature move charges.

An optical sampling head is discussed in much more detail in [2]. The basic idea is that the incident beam is polarized in

Manuscript received October 24, 1994; revised March 20, 1996. This work was supported by the Army Research Office under Grant #DAAL-03-92-G-0289 and by the Office of Naval Research under Grant #DOD-ONRN00014-92-J-1190.

The authors are with the Department of Electrical and Computer Engineering, University of Colorado at Boulder, Boulder, CO 80309-0425 USA.

Publisher Item Identifier S 0018-9480(96)04700-X.

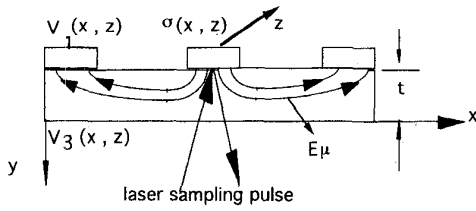


Fig. 1. Schematic depiction of the device under test defining the coordinate system and sampling geometry.  $V_1(x, z)$  is the potential on the top surface of the active antenna and  $V_3(x, z)$  is the potential on the back surface of the substrate.

an elliptical state that is maximally sensitive to the effect of the electrooptic coefficient of the GaAs substrate. The microwave electric field in the substrate, through the electrooptic coefficient, induces a rotation in the polarization state, which is then read out by an analyzer placed in front of a slow detector. The magnitude and phase of the signal received by the detector will then be proportional to a voltage defined by

$$V_{eo} = \text{const.} \int E_{\mu}(x, y, z) d\ell \quad (1)$$

where  $V_{eo}$  is the electrooptic voltage,  $E_{\mu}$  is the microwave field and  $x, y, z$  and  $\ell$  are defined in Fig. 1. From Fig. 1, it is quite evident that the measured signal will be a function of the thickness  $t$  of the sample. However, there are two limits in which the measured quantity becomes directly proportional to physical quantities. Clearly, for a sufficiently thick sample, the voltage  $V_3(x)$  of Fig. 1, will approach the reference potential at infinity (ground) and the measured  $V_{eo}(x, z)$  will become identical with the potential  $V_1(x)$  of the top surface. Additionally, in the limit where the sample thickness becomes small, the optical wave will see only the normal component of  $E_{\mu}$  evaluated at  $E_{\mu}(x, y = 0, z)$ , which will then be directly proportional to  $\sigma$ , the surface charge density on the upper surface electrodes. In the next section, we will see that measurements for microwave circuits with arbitrary substrate thickness  $t$  are sufficient to determine both  $\sigma$  and  $V_1$ .

### III. MATHEMATICAL RELATIONS BETWEEN THE POTENTIAL AND CHARGE DISTRIBUTIONS

For a simple coplanar waveguide (CPW) transmission line (Fig. 1), where the characteristic dimensions of the line are sufficiently small in units of the wavelength one can use the quasi-static limit (see, for example, [4]). In the case where the wave distributions, that is the voltage and charge distributions, are purely forward propagating, i.e., an ideal matched microwave transmission line, one could simply write that

$$V(x, z, t) = aV_{QS}(x, z)e^{i\beta z}e^{-i\omega t} \quad (2a)$$

$$\sigma(x, z, t) = a\sigma_{QS}(x, z)e^{-i\beta z}e^{-i\omega t}. \quad (2b)$$

If one considers the specific case as illustrated in Fig. 1 the quasi-static limit yields [3]

$$\begin{aligned} V_{eo}(x, z) &= V_1(x, z) - V_3(x, z) \\ &= \int G(x, x', z, z')\sigma(x', z') dx' dz' \end{aligned} \quad (3)$$

where  $V_1(x, z)$  is the potential on the top surface of the sample,  $V_3(x, z)$  is the potential on the bottom surface of the sample and the Green's function (see [5] for in depth discussions of Green functions) can be deduced from the expressions for the potentials. The  $V_1(x, z)$  and  $V_3(x, z)$  are then given by [6]

$$\begin{aligned} V_1(x, z) &= \frac{\sigma}{4\pi\epsilon} \int_0^{\infty} J_0(kr)e^{-k|z|} dk \\ &+ \int_0^{\infty} \phi(k)J_0(kr)e^{kz} dk \end{aligned} \quad (4)$$

and

$$V_3(x, z) = \frac{(1 - \beta^2)\sigma}{4\pi\epsilon} \int_0^{\infty} \frac{J_0(kr)e^{-kt}}{1 - \beta e^{-kt}} dk \quad (5)$$

where

$$\phi(k) = \frac{\beta(e^{-2kt} - 1)}{1 - \beta^2 e^{-2kt}}, \quad (6)$$

$$r = \sqrt{(x - x')^2 + (z - z')^2} \quad (7)$$

$$\beta = \frac{\epsilon_r - 1}{\epsilon_r + 1} \quad (8)$$

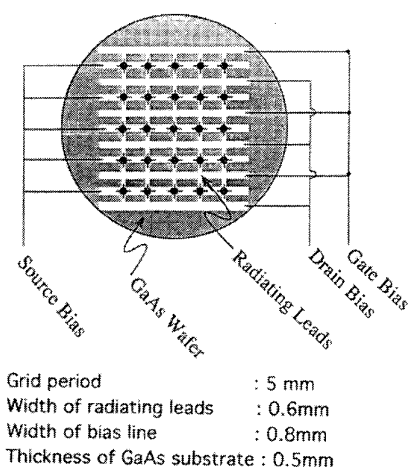
with  $\epsilon_r$  being the relative substrate permittivity.

After obtaining calibrated measurement data for  $V_{\infty}(x, z)$ , one can use standard numerical techniques to invert (3) and obtain  $\sigma(x, z)$ , the charge distribution. One can then use relations in (3) and (4) to determine the front and backside potentials. Results of this procedure will be presented in Section V of this paper. First however, some discussion will be given to the test structure.

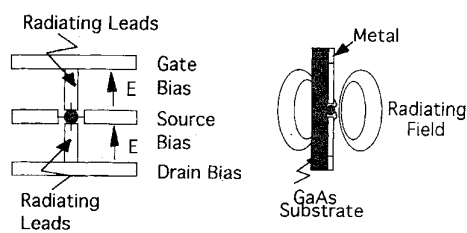
### IV. AN ACTIVE ANTENNA

What we really mean here by an active surface is one that contains active devices and through the action of these devices performs some operation on waves incident perpendicularly to the surface. This operation could be generation, amplification, filtering, mixing or some other operation. Perhaps the simplest example of an active surface would be that of an active antenna, that is, a radiating element in which an active element is used for frequency adaptive loading. The implementation of such antennas is not a recent development. Experimental results on such antennas had already appeared in literature by 1928 [7], where the loading active element was a triode. A number of papers appeared in this field in the early 1970's [8]–[12], likely spurred by the development of high frequency transistors and hoping to increase bandwidth [13], make short antennas effectively longer [14], [15], or to decrease mutual coupling between array elements [16] through using the transistor as an impedance transformer with gain. More recently, attention has turned to self-oscillating active arrays for power combining [17]–[22].

In the experiment presented in this paper, both a single active antenna and an active power combining array were constructed on a semi-insulating undoped GaAs. (The array structure of such an oscillator built on a duroid substrate was previously investigated for quasi-optical power combining



(a)



(b)

Fig. 2. (a) The structure of an archetypal active antenna array and (b) a structure of a single active antenna.

[18].) The thickness of the GaAs ( $\epsilon_r = 12.5$ ) wafer is  $500 \mu\text{m}$ . Fig. 2(a) and (b) show the structure of an archetypal active antenna array and structure of a single active antenna. The metallization on the GaAs was performed using a standard photolithography technique. First, a  $100 \text{ \AA}$  of titanium was evaporated on the substrate as an adhesion layer. This was followed by  $100 \text{ \AA}$  of gold evaporated onto the titanium and then plating the gold to a thickness of  $1.5 \mu\text{m}$ . Finally, HEMT's and MESFET's in chip form (Fujitsu FHX35X, and FHX02x) were epoxied onto the metallized substrate using opo-tk70 epoxy (chosen for its high thermal conductivity). These chips were used as the active elements because of their gain at high frequencies. The gate, drain and source pads on the chip were bonded to plated leads using thermal compression.

Various sizes (from  $1 \times 1$  to  $5 \times 5$ ) of active antenna arrays were built by the fabrication procedure described above. The microwave characteristics of these active antennas were tested before optical sampling was performed. The 25 HEMT array oscillated at 5.89 GHz with mirror feedback and bias voltages of  $V_{gs} = -0.6 \text{ V}$  and  $V_{ds} = 0.6 \text{ V}$ , respectively. Polarization of the radiation field is mainly along the gate and drain leads. Radiation fields in the cross polarization state along the bias lines are about 20 dB less. The oscillation frequency of the grid is strongly related to the drain and source bias dc current  $I_{ds}$ . When the total  $I_{ds}$  was smaller than 12.8 mA, the grid oscillated at 5.27 GHz. When the total current  $I_{ds}$  was larger than 12.8 mA, the oscillation frequency stabilized at 5.9 GHz. Increasing the current  $I_{ds}$  to approximately 15.7 mA

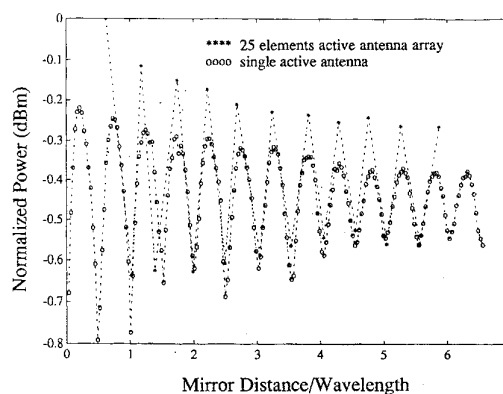


Fig. 3. The comparison of the shape of the radiated power versus mirror distance curves for both single elements and active antenna arrays. Note that the powers are not normalized to the same scale.

caused the oscillation frequency to increase to 7.0 GHz with other lower unsuppressed frequencies also present. Changes in either the bias voltages or the mirror position changed the current  $I_{ds}$ , which in turn affected the oscillation frequency of the oscillator. The injection locking range of the 25 HEMT array is about 2 MHz around the center frequency. The  $1 \times 1$  single active HEMT antenna has very similar microwave characteristics to the  $5 \times 5$  HEMT antenna array. It oscillated around 5.8 GHz when biased at the same bias conditions as the 25 element array. Fig. 3 shows the comparison of the radiated power between the 25 HEMT element array and a single active HEMT antenna versus the mirror distance. (Please note the comparison is of the zero crossings and not the amplitudes as the two amplitudes are not scaled the same way). We can see that the effect of the mirror feedback is similar in the two cases. Ferrite beads were used to avoid the usual RF reception problems and the DC bias was fed to the array by a high stability Hewlett Packard power supply with small inductance wires soldered on to the end of the array at the bias lines. A very exhaustive discussion of the general grid oscillator including mirror feedback effects can be found in [19].

Another single active antenna was built on the same passive circuit structure but using a Fujitsu MESFET's FHX02x. This active antenna oscillated at 6.78 GHz at the bias condition of  $V_{gs} = -0.5 \text{ V}$ ,  $V_{ds} = 0.4 \text{ V}$ . The effect of different active elements in the same passive structure not only changed the radiation frequency, but also changed the radiated power of the active antenna. Even though these two antennas radiate at different power levels and different frequencies, the effect of the mirror feedback to power level of the antennas is the same. Fig. 4 shows the oscillation frequencies of the active antennas versus the mirror distance. We observed that the oscillation frequencies are almost constant as we move the mirror beyond the distance of half of the wavelength away from the device. This means that the effect of the mirror on the oscillation frequency is minor if the mirror is more than one wavelength away from the device, at least in the case where both the individual devices and their spacing are much less than a wavelength. These results show that the self-oscillating conditions are mainly determined by the near field

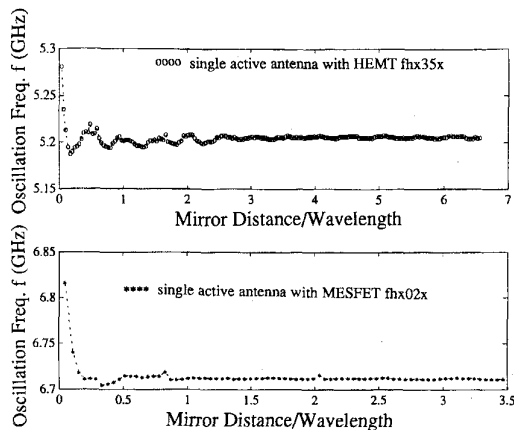


Fig. 4. The oscillation frequencies of single active antenna versus mirror distance.

radiation effects on the antenna structure, not by the mirror feedback. In other words, the coupling effects of the element to element oscillators swamp the mirror feedback effects when the mirror is more than one wavelength away. The effect of near field radiation to the charge distribution of the active antenna can only be obtained from noninvasive electrooptical sampling measurements.

#### V. OPTICAL SAMPLING MEASUREMENTS

A radiating microwave oscillator can have its oscillation frequency affected by disturbances from nearby surroundings. Since the electrooptic sampling measurement apparatus effectively heterodynes the laser pulse signal and the microwave signal inside an electrooptic substrate, microwave injection locking to the laser mode locker is necessary. Precise synchronism between the laser pulse and microwave device is necessary since slight drifts in frequency (of the test microwave device) away from the harmonic of the laser pulse in a sampling measurement will produce inaccurate results due to the narrow bandwidth (1 MHz) used in the detector/amplifier. The principle of optical sampling arrangement for measuring the amplitude and phase of the potential is illustrated in [1] and [2]. The detailed experimental set-up for the active devices is shown in Fig. 5. A 10 dB microwave directional coupler was used to separate the injected signal and the detected signal of the active array structure. A spectrum analyzer is used to monitor the injection process while conducting optical sampling and is also used to record the output signals of the probe beam collected by a detector/amplifier while sending this data to a computer. During real time measurements, the probe beam scans the active structure. Polarization of the probe beam will change its direction due to the local potential difference of both sides of the substrate, which modulates the intensity of the optical beam. The relative phase in the potential distribution can also be measured by feeding the laser reference and reflected beam to a lock-in amplifier that heterodynes the two signals. Calibration of the electrooptic signal, due to small thickness variations across the wafer, is done by comparing the direct current optical power to the reflected beam as the scanning is performed. In general, calibrations relevant to the

#### ELECTROOPTIC SAMPLING MEASUREMENT SYSTEM

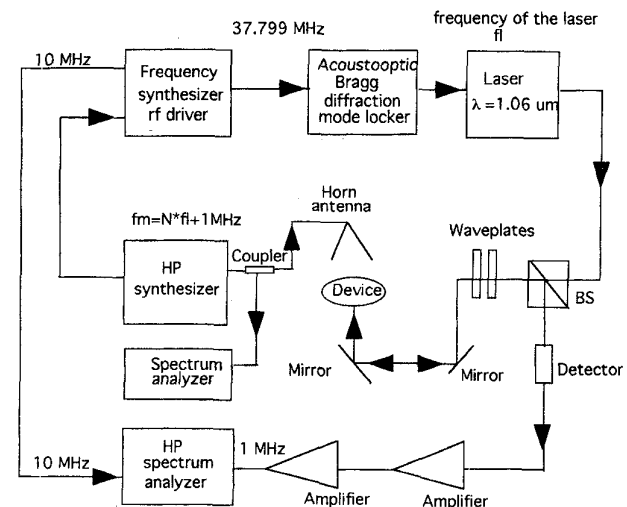


Fig. 5. The optical sampling arrangement for measuring the amplitude of potential distribution of active antennas.

measurements are made by making “known” test structures on the same substrate as the device under test and scanning these structures to determine the calibration parameters [1].

As was discussed, the polarization of the probe beam is rotated in proportion to the complex value of the relative potential on the structure due to the electrooptic coefficient of GaAs. Therefore, measurements of the potential distribution while the active antenna array is oscillating can be made. The in-situ measurement is realized by injection locking the oscillation frequency of the active antenna array to one of the components of the mode locked laser pulse. In order to stabilize the oscillation frequency of the active antenna array, the frequency of the array was adjusted to around 5.89 GHz. A broadband horn antenna was placed approximately 30 cm away from the active antenna structure. Thus, the horn antenna was able to injection lock the structure at 5.8967 GHz. This frequency was then synchronized with the 78th harmonic of the laser pulse to within a receiver bandwidth of 1 MHz.

Fig. 6(a)–(d) show some of the measured potential distributions along a column of the active HEMT array obtained from the noninvasive optical sampling apparatus. The data was taken in real time with the array oscillating at 5.8967 GHz and represents the potential difference between front and back sides of the GaAs wafer. A higher potential is measured where the drain and gate leads are close to the active devices. A 180° phase shift was measured across the active devices. The maximum value of the potential in the drain is slightly higher than the one in the gate, displaying much lower potential values in the source leads even at points close to the HEMT. The measured potential values on the source leads close to the active element are nonzero, but their maximum is significantly lower than those of the gate or drain leads shown in Fig. 6(e). Optical sampling results reveal a zero relative potential difference between the gate and drain bias lines [shown in Fig. 6(f)]. Fig. 6(g) shows the 2-D distribution of the potential in

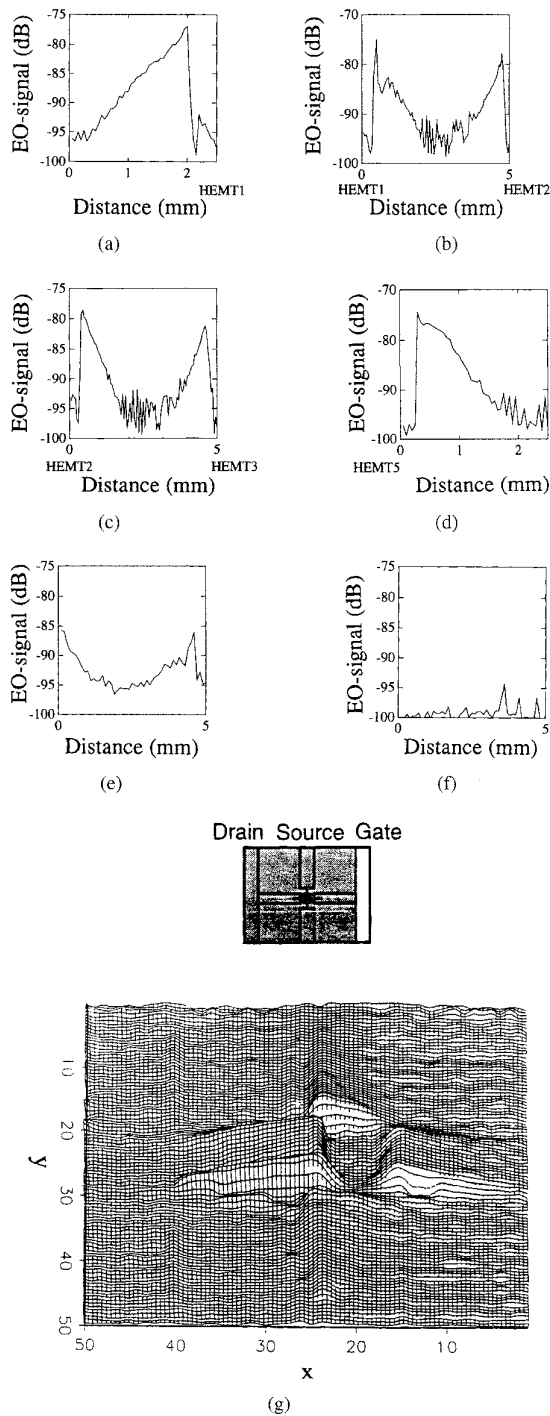


Fig. 6. Some of the measured potential distributions along a column of the active HEMT array are obtained from the noninvasive optical sampling. (a)–(d) The potential along the drain and gate radiating leads, (e) the potential along the source bias lead, (f) the potential along the gate bias lead, and (g) the 2-D distribution of the potential in an elementary cell of the 25 HEMT arrays.

a cell of the 25 HEMT element arrays. These results depict some unusual features of active antenna structures when they are under a large signal operation. Of particular interest is the complete absence of boundary effects near the center bias lines.

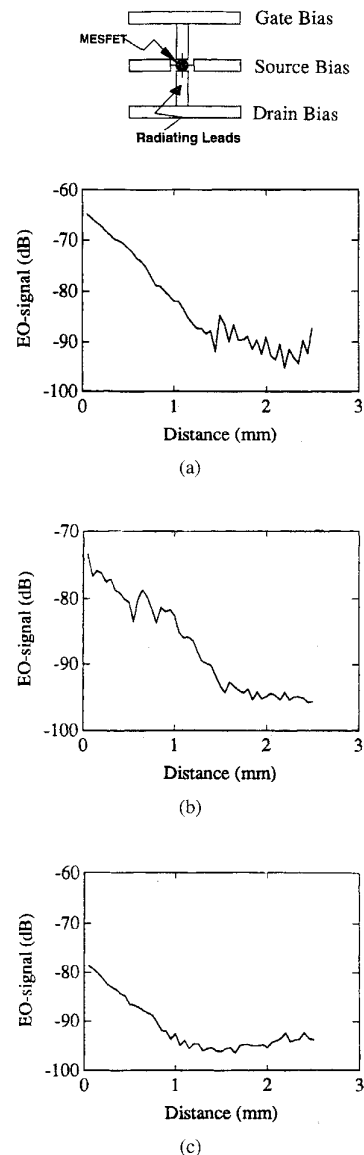


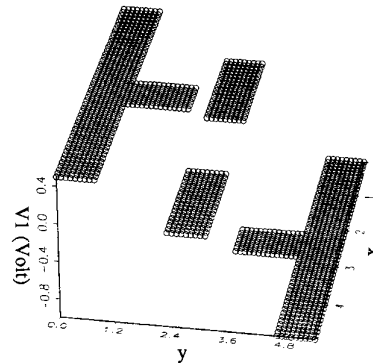
Fig. 7. Measurements of the potential distribution of a single MESFET active antenna. (a) Potential along the drain radiating lead. (b) Potential along the gate radiating lead, and (c) potential along the source bias line.

The measured potential distributions of all cells in the active structure were found to exhibit remarkably similar forms. Only the magnitudes of the potential distributions vary slightly from one transistor to the next, possibly due to nonidentical transistors. Removing a HEMT from the array did not affect the potential distribution in an adjacent cell. Further evidence of the independence of these structures manifests itself in the measurements across a single active antenna ( $1 \times 1$ ). In this case, the distribution is similar to that of a single unit cell placed in an entire active antenna array. Measurements of the potential distribution of a single cell are illustrated in Fig. 7(a)–(c). It is interesting to note, that the potential appears qualitatively quite similar to any of the cells that were connected together in the array structure. It is almost as if the elements of the array structure act independently of one another.

## VI. ANALYSIS OF MEASUREMENT DATA

As was previously mentioned, the actual quantity measured by optical sampling,  $dV$ , is the potential difference between the front and back of the substrate. As in the present case, the structure is operating in the radiating mode. The dimension of the elementary cell is  $5 \times 5 \text{ mm}^2$ , the width of the electrodes are about 0.8 mm and the sample thickness is 0.5 mm, one would assume there could be significant potential on the back surface of the substrate. Therefore, the potential distribution on the electrode  $V_1$ , will be different from the measured potential  $dV$ . Since our measurement data has shown such remarkable similarity between the elementary cell of the array and the single active antenna, the single antenna can be used as an example for finding the actual potentials from the measurement. In order to recover the potential distribution  $V_1$ , the Green's function derived in Section II is used in the calculation. It is noted that the normalized measurement potential  $dV$  has noise floor at 0.1 V, which means that any  $dV$  value on the antenna lower than 0.1 V will be detected as noise. Our simulations have shown that the exact potential value on the noise floor will effect the actual distribution of  $V_1$  on the electrodes. Direct inversion of (4) will not be especially accurate. To recover the actual potential distribution from the measurement as accurately as possible, an expression of the distribution  $V_1$  has to be estimated first. We will presently develop a procedure to evaluate the possible distributions of  $V_1$ . The structure of the active antenna consists of three bias lines [shown in Fig. 2(b)] which form three coplanar lines. These lines can support two fundamental modes, one an even mode [0 1 0], the other an odd mode [-1 0 1]. Any operation mode of this structure must be a combination of these two modes. Knowing that the antenna is a radiating structure, the dominant mode of the structure must be an odd mode. Due to the  $180^\circ$  phase shift crossing the active element, opposite charges on both sides of the active device will tend to cancel out their effect on the potential on the back of substrate  $V_3$ . This results in  $V_3$  having minimum magnitude near the active device, and increased magnitude as one moves away from the active device. Hence, the correction in  $V_1$  from the measured value  $dV$  is small near the active device. Away from the active device region, the difference between  $V_1$  and  $dV$  could be large. This depends on the charge distribution. In light of the experimental results, various 2-D-potential distributions of  $V_1$  under odd dominant mode operation are assumed. The 2-D-distributions of  $dV$  in these cases are calculated from the distributions of  $V_1$  using the Green's function derived in Section II and the method of moments. The calculated 2-D-distributions of  $dV$  will then be compared with the measurements. Since the experimental value has noise floor at 0.1 V, the calculated distributions will also use 0.1 V as noise floor value.

We have studied five possible cases [24]. In cases 1 and 2, uniform potential distributions on the drain ( $V_d$ ), source ( $V_s$ ), gate ( $V_g$ ) bias lines and the gate, drain radiating leads are assumed (shown in Fig. 8). In case 1, potentials are set to  $[V_g, V_d, V_s] = [0.5 \text{ V}, 0 \text{ V}, -1 \text{ V}]$  and in case 2 potentials are set to  $[V_g, V_d, V_s] = [0.525 \text{ V}, 0.25 \text{ V}, -1.25$

Fig. 8. Two-dimensional potential distribution of  $V_1$  in cases 1–2.TABLE I  
COMPARISON OF CALCULATED POTENTIAL  
DISTRIBUTION FROM THE MEASURED DISTRIBUTION

Case Number	Standard Deviation $\sigma_{sd}$	Maximum Deviation $\max(\sigma_{sd})$
case 1	0.0858	0.4840
case 2	0.1034	0.4128
case 3	0.0368	0.2234
case 4	0.0418	0.2780
case 5	0.0358	0.1940

V]. Potential distributions of  $V_1$  in cases 3–4 are similar to the cases 1–2, except that the potentials along the gate and drain radiating leads decrease linearly from the active device. Potential distributions of  $V_1$  in case 5 are assumed to decrease linearly along the gate and drain radiating leads as well as the source bias line from the active device. The calculated  $dV$  distributions from these five cases are compared with the measured 2-D  $dV$  distribution. From the experiment, the total numbers of sample points,  $nq = 1420$ , are taken from the electrodes of the antenna and each sampling increment step is  $100 \mu\text{m}$ . Therefore, the calculated  $dV$  is also arranged so that there are a total of 1420 calculated points and each increment step is  $100 \mu\text{m}$ . The standard deviation of the calculated  $dV_c$  from the measured  $dV_m$  is defined as

$$\begin{aligned} \sigma_{sd}^2 &= \frac{1}{nq} \sum_{i=1}^{i=nq} \sigma_{sdi}^2 \\ &= \frac{1}{nq} \sum_{i=1}^{i=nq} (dV_{ci} - dV_{mi})^2 \end{aligned} \quad (9)$$

where,  $dV_{ci}$  is the calculated potential of  $dV$ ,  $dV_{mi}$  is the measured potential of  $dV$  and  $\max(\sigma_{sdi})$  is the maximum value among the  $\sigma_{sdi}$ . The results of these comparisons are shown in Table I.

Note that cases 1–2 have assumed a uniform distribution of  $V_1$ , in the gate, drain, and source regions. The assumption for this type of distribution fits poorly to the experimental results (measurement error from the experiment due to the noise is lower than 4.3%). Both the standard deviation and maximum deviation are nearly twice as large as other cases. The difference between cases 1–2 is indistinguishable. The

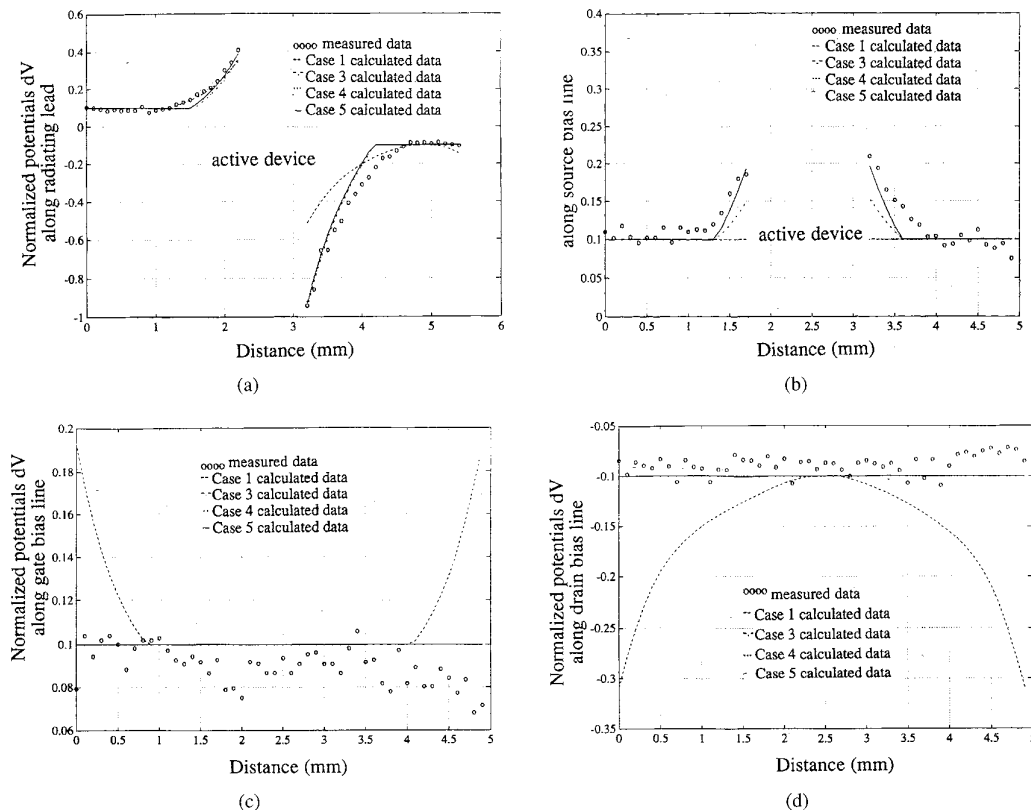


Fig. 9. Comparison of measured potential  $dV$  with calculated potential  $dV$  from four different cases. (a) Distributions on the radiating leads at both sides of the active device, (b) distributions on the source bias lines, (c) distributions on the gate bias line, and (d) distribution on the drain bias lines.

best fit potential distribution is the one in case 5. In this particular case, the potential distribution is assumed as linearly decaying throughout the radiating lead and the source lead. The second best fit is followed by case 3, then case 4. Fig. 9(a)–(d) show the comparison of the calculated potential and the measured potential. These 1-D plots have presented the same results as shown in Table I. As is seen, there is a definite correction of  $V_1$  from  $dV$ . In case 5, the correction for  $V_1$  is not more than 20% of the  $dV = V_1 - V_3$  curve, but the correction for  $V_1$  is more than 400% in case 1. In the following section, discussion will be given as to possible explanations for these distributions.

## VII. DISCUSSION

In Sections V and VI, we have presented the results of the measurements and have analyzed these results using numerical simulations. Because of the radiating nature of the structure, the electric fields are not strongly confined in the sample. Furthermore, since the substrate is thin in comparison to the linewidth, the sample measurements are more sensitive to the charge distribution than the potential distribution as was discussed in Section II. The change in the measured distribution of  $dV$  is therefore not as sensitive to variations of the charge distributions in  $V_1$ . A reasonable fit of the distribution of  $V_1$  from the measured data will not be unique. Therefore, caution must be employed in interpreting the measurement results. The purpose of the following discussion is to obtain a

self-consistent modeling that can explain the measured data we obtained from both the single element and the array antenna.

Comparisons of the calculated distributions of  $dV$  from all five cases of measured data show that uniform potential models of  $V_1$  (the classic distribution for capacitive loaded dipole) have the largest standard derivation. The values of 8.58–10.34% are well above the measurement error (which is  $<4.3\%$ ). This means that the uniform potential distribution approximation for the active antenna does not fit well with our experimental results. In contrast, the linearly decaying models used in cases 3–5, have an average standard deviation below the measurement error. Among them, the model in case 5 has the lowest value for the maximum deviation of the measurement value. The plot in Fig. 9 shows that the model of case 5 agrees well with the experimental measurement. The model of case 3 also shows agreement with the measured data in the radiating leads and the bias line. However, the fitting in the source bias line is not as good as the one from case 5. The same conclusion can also apply to case 4. As we remember, along the radiating lead of the antenna the distribution of  $V_1$  is assumed to be linearly decaying from the active device in these three cases. In cases 3 and 5, the potential is made to decay to zero on the gate and drain bias lines, but in case 4 some residual value of the potential is set on both of the bias lines. From symmetry there is some motivation to assume that there would be zeros on the

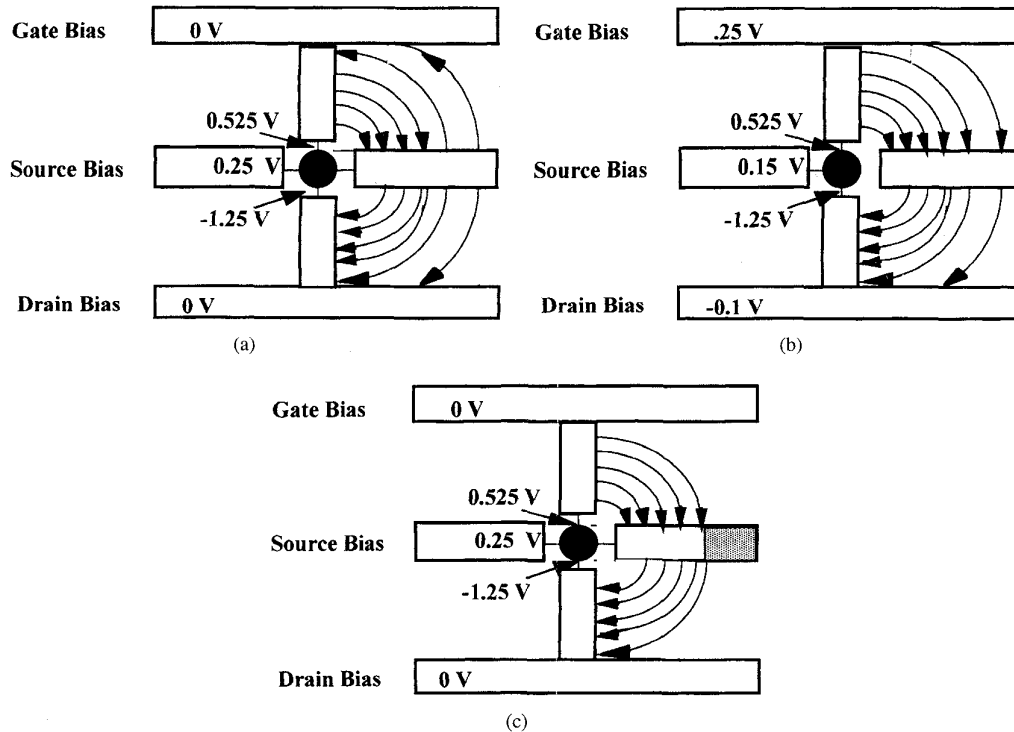


Fig. 10. The schematic diagrams of the potential distributions and the main field lines presented in (a) case 3, in (b) case 4, and in (c) case 5.

bias lines. For the distribution of  $V_1$  on the source bias line constant distributions are considered in cases 3 and 4, and the linearly decaying potential from the active device is assumed in case 5. In case 5, the value of  $V_1$  on the source line will reach zero at the place where the distance from the active device is larger than the length of the radiating leads. Even though the potential distributions in cases 3–5 are similar, they represent different modes of operation. Fig. 10(a)–(c), show the schematic diagrams of the potential distributions and the main field lines in cases 3–5. As we can see, the antenna is dominated by the odd mode in the region near the active device in all cases. Therefore, the radiating fields of the antenna are polarized along radiating leads. However, away from the active device, the field lines are different for different cases. Fig. 10(a) shows that an even (guided) mode is formed in the bias lines. Thus, some energy will guide along the bias lines in this particular case. Fig. 10(b) shows that the odd mode continues to dominate in case 4. Some energy will also be guided on the bias lines, but radiation losses will be larger than the ones in case 3. Fig. 10(c) shows there will be no energy guided along the bias lines so that all the energy will radiate into free space in case 5. The approximated potential distributions from these three cases have common characteristics, that is, most of the field strength is clustered around the region near the active device. At a place further away from the active device, the field strength is weaker. This indicates that the near fields have the strongest influence on the circuit parameters as well as the oscillation condition of the antenna. That explains why the microwave characteristics of the single active antenna are similar to the ones in the array. It is also noted that the magnitude of excitation voltage in the

gate terminal of the active device is smaller than the drain, here the active antenna is always somewhat asymmetrically excited.

The decaying potential on the radiating lead can be explained as follows: The bias lines for the active device terminals can be viewed as coplanar lines. In order for the antenna to radiate energy into space, the odd mode (radiated mode) must be the dominant mode for these coplanar lines. The radiating leads are in a position perpendicular to the bias lines but parallel to the polarized direction of the radiated field, therefore, the radiating leads appear to be inductive to the ac current of the active device. This distributed inductance is the main reason for the ac potential decay along the radiated leads. Even though the cross polarized field is 20 dB lower than the main one, the field has polarization along the bias lines. This has the same effect for the ac potential along the source line, and the potential on the source bias line could have linearly decaying behavior. Furthermore, as the transistor resonates, a large amount of phase shift takes place inside the active device. This may explain why the active antenna will resonate at a length much smaller than half of the oscillation wavelength.

Now, a remaining question might be will the potential distribution decay to zero as it reaches to the bias line as suggested in the models in cases 3 and 5? or, will it decay to some non-zero value as predicted in case 4? Due to the radiating nature of the active antenna, we have progressively lower signal to noise ratios as we sample farther away from the active device. Noise peaks cause about 4.3% measurement uncertainty. The 4.3% measurement uncertainty in the noise floor will not allow us enough sensitivity to distinguish between the three possible distributions of cases 3–5.

If a single active antenna has potential distributions as those presented in cases 3 and 5 then the potential distributions decay along the radiating leads to zero at gate and drain bias lines. Although the global potential distribution of a column of an active antenna array from cases 3 and 5 will be dramatically different from the distributions suggested in case 4, the optical sampling measurement for the global amplitude measurement of  $dV$  will not be that different between these three cases. One of the reasons is that the GaAs substrate used is quite thin compared to the size of the active antenna. The probe beam can only be sensitive to the difference in the local field (generally, within the elementary cell). However, the difference in the above three cases can be easily distinguished by the phase measurement of the potential. If an elementary cell has the potential distributions of cases 3 and 5,  $180^\circ$  phase shifts can be easily detected as the probe beam scans across each active device in a column of the active array. However, there will be no phase shift for each active device in the distribution presented by case 4. Hence, the model in case 4 can be eliminated.

Combined with all the information obtained from the experiments, our results suggest that the potential distribution presented in cases 3 and 5 for a single active antenna are the most appropriate solutions. So far, our experiment is not accurate enough to distinguish cases 3 from 5.

### VIII. SUMMARY

In the present work, various active antennas have been fabricated on GaAs substrates, and the microwave characteristics of the antennas were tested. The noninvasive, in-situ optical sampling technique has been used to obtain the potential distributions on the active antennas. Based on our experimental results and numerical simulations, the potential distribution models were developed to describe the experimentally observed phenomena. These calculated potential distributions agree well with the measured results. From this study of these active antennas, we have uncovered information concerning the dynamic behavior of active devices. More specifically, we have observed that the uniform potential distribution assumed for an "ideal" small dipole is not the case for a small active antenna. Oscillation conditions for such active arrays of such elements seem to be governed by their near field distributions instead of the field boundary conditions imposed by their neighbors.

### ACKNOWLEDGMENT

The authors are grateful to D. Pannan of the Ball Aerospace Co. for his help with device bounding. The authors also wish to thank Dr. D. H. Hjelme for his set-up of the optical sampling and useful discussions.

### REFERENCES

- [1] D. R. Hjelme and A. R. Mickelson, "Voltage calibration of the direct electrooptic sampling technique," *IEEE Trans. Microwave Theory Tech.*, vol. 40, pp. 1941–1950, Oct. 1992.
- [2] D. R. Hjelme, M. J. Yadlowsky, and A. R. Mickelson, "Two-dimensional mapping of microwave potential on MMIC's using electrooptic sampling," *IEEE Trans. Microwave Theory Tech.*, vol. 41, pp. 1149–1158, June/July 1993.
- [3] V. Radisic, D. Hjelme, A. Horrigan, Z. Popovic, and A. R. Mickelson, "Experimentally verifiable modeling of coplanar waveguide discontinuities," *IEEE Trans. Microwave Theory Tech.*, vol. 41, pp. 1524–1533, Sept. 1993.
- [4] Pocklington, "Electrical oscillation in wires," in *Proc. of the Cambridge Philosophical Society*, 1897, pp. 324–333.
- [5] I. Stackgold, *Boundary Value Problems of Mathematical Physics, I and II*. London: Macmillan, 1972.
- [6] W. R. Smyth, *Static and Dynamic Electricity*. New York: Hemisphere, 1989.
- [7] This 1928 work is referenced in J. H. Dunlavy and B. C. Reynolds, "Electrically small antennas," in *23rd Annual USAF Antenna Research and Development Symp.*, Univ. of Illinois, Oct. 1973.
- [8] H. A. Wheeler, "Small antenna," *IEEE Trans. Antennas Propagat.*, vol. 23, pp. 462–469, 1975.
- [9] A. P. Anderson, W. S. Davies, M. M. Dawond, and P. E. Galanakis, "Note on transistor-fed active-array antennas," *IEEE Trans. Antennas Propagat.*, vol. 19, pp. 537–539, July 1971.
- [10] A. P. Anderson and M. M. Dawond, "The performance of transistor fed monopoles in active antennas," *IEEE Trans. Antennas Propagat.*, vol. 21, pp. 371–374, May 1973.
- [11] P. L. Fanson and K.-M. Chen, "Instabilities and resonances of actively and passively loaded antennas," *IEEE Trans. Antennas Propagat.*, vol. 22, pp. 342–347, Mar. 1974.
- [12] J. P. Daniel, "Mutual coupling between antennas for emission or reception—Application to passive and active dipoles," *IEEE Trans. Antennas Propagat.*, vol. 22, pp. 347–349, Mar. 1974.
- [13] M. I. Kontorovich and N. M. Lyapunova, "Active antennas," *Radio Eng. Electron. Phys.*, vol. 19, pp. 126–127, 1974.
- [14] M. Dawond and A. P. Anderson, "Calculations showing the reduction in the frequency dependence of a two-element array antenna fed by microwave transistors," *IEEE Trans. Antennas Propagat.*, vol. 20, pp. 497–499, 1972.
- [15] T. S. Maclean and P. A. Ransdale, "Short active aerials for transmission," *Int. J. Electron.*, vol. 36, no. 2, pp. 261–269, Feb. 1974.
- [16] P. K. Rangole and S. S. Midha, "Short antenna with active inductance," *Elec. Lett.*, vol. 10, pp. 462–463, Oct. 1974.
- [17] J. P. Daniel and C. Terret, "Mutual coupling between antennas—optimization of transistor parameters in active antenna design," *IEEE Trans. Antennas Propagat.*, vol. 23, pp. 513–516, July 1975.
- [18] J. W. Mink, "Quasi-optical power combining of solid-state millimeter-wave sources," *IEEE Trans. Microwave Theory Tech.*, vol. 34, pp. 273–279, Feb. 1986.
- [19] Z. Popovic, R. M. Weikle, II, M. Kim, and D. B. Rutledge, "A 100-MESFET planar grid oscillator," *IEEE Trans. Microwave Theory Tech.*, vol. 39, pp. 193–200, 1991.
- [20] J. Birkeland and T. Itoh, "A 16 element quasi-optical FET oscillator power combining array with external injection locking," *IEEE Trans. Microwave Theory Tech.*, vol. 40, pp. 475–481, Mar. 1992.
- [21] R. A. York and R. C. Compton, "Quasi-optical power combining using mutually synchronized oscillator arrays," *IEEE Trans. Microwave Theory Tech.*, vol. 39, pp. 1000–1009, June 1991.
- [22] K. Chang, K. Hummer, and J. L. Klein, "Experiments on injection locking of active antenna elements for active phased arrays and spatial power combiners," *IEEE Trans. Microwave Theory Tech.*, vol. 37, pp. 1078–1084, July 1989.
- [23] N. Camilleri and B. Bayraktakoglu, "Monolithic millimeter-wave IMPATT oscillator and active antenna," *IEEE Trans. Microwave Theory Tech.*, vol. 36, pp. 1670–1676, Dec. 1988.
- [24] K. Y. Chen, "Active antenna and periodic structures," Ph.D. dissertation, Univ. of Colorado at Boulder.

**Kuang Yi Chen**, photograph and biography not available at the time of publication.